

First-principles study of lattice instabilities in the ferromagnetic martensite Ni₂MnGa

Claudia Bungaro* and K. M. Rabe

Department of Physics and Astronomy, Rutgers University, Piscataway, NJ 08854-8019, USA.

A. Dal Corso

Scuola Internazionale Superiore di Studi Avanzati (SISSA), Via Beirut 2/4, 34014 Trieste, Italy.

The phonon dispersion relations and elastic constants for ferromagnetic Ni₂MnGa in the cubic and tetragonally distorted Heusler structures are computed using density-functional and density-functional perturbation theory within the spin-polarized generalized-gradient approximation. For $0.9 < c/a < 1.06$, the TA₂ transverse acoustic branch along [110] and symmetry-related directions displays a dynamical instability at a wavevector that depends on c/a . Through examination of the Fermi-surface nesting and electron-phonon coupling, this is identified as a Kohn anomaly. In the parent cubic phase the computed tetragonal shear elastic constant, $C'=(C_{11}-C_{12})/2$, is close to zero, indicating a marginal elastic instability towards a uniform tetragonal distortion. We conclude that the cubic Heusler structure is unstable against a family of energy-lowering distortions produced by the coupling between a uniform tetragonal distortion and the corresponding [110] modulation. The computed relation between the c/a ratio and the modulation wavevector is in excellent agreement with structural data on the premartensitic ($c/a = 1$) and martensitic ($c/a = 0.94$) phases of Ni₂MnGa.

I. INTRODUCTION

Ferromagnetic shape-memory alloys displaying large magnetic-field-induced strain have recently emerged as a new class of active materials, very promising for actuator and sensor applications. The largest known magnetostrain effects have been observed in Ni₂MnGa-based Heusler alloys, where up to 6% and 9.5% strains have been induced by a magnetic field less than 1 Tesla.^{1,2}

The magnetic shape-memory behavior is closely linked to the occurrence of a martensitic transformation in conjunction with a strong magnetocrystalline anisotropy of the low-temperature martensitic phase. For a deeper understanding of the magnetic shape-memory mechanism, a microscopic explanation for the origin of the martensitic transformation and the magnetocrystalline anisotropy is clearly needed. Towards this goal, we have used *ab initio* techniques to investigate the origin of the martensitic transformation.

Ni₂MnGa is the most intensively studied of the relatively few known ferromagnetic shape-memory materials. A number of thermal and stress-induced martensitic transformations have been observed in Ni₂MnGa-based alloys, and both transition temperatures and crystallographic structures are quite sensitive to alloy composition.

In the stoichiometric alloy, Ni₂MnGa, which is ferromagnetic below $T_C \approx 380$ K, two thermally-induced phase transitions have been observed. From the high-temperature cubic Heusler structure, a premartensitic phase transformation to a modulated cubic structure occurs below $T_{PM} \approx 260$ K,^{3,4} followed by a martensitic transformation to a modulated tetragonal structure below $T_M \approx 220$ K.⁵ The low temperature martensitic phase has a tetragonal structure ($c/a=0.94$, $a=5.90\text{\AA}$) with a superimposed incommensurate modulation along the [110] direction, consisting of a shuffling of (110) planes in the $[\bar{1}10]$ direction with a periodicity of almost 5 interplanar distances, which corresponds to a wave vector $\mathbf{q}_M \approx \frac{2\pi}{a}(0.43, 0.43, 0)$ (Refs. 4, 6). The low-temperature martensitic phase has a high magnetocrystalline anisotropy,⁷ making it useful for applications. At a phenomenological level, the coupling between strain, modulation, and magnetization has recently been described in a Landau-theory framework.⁸

Some clues to the microscopic origin of the martensitic transitions are provided by the softening of particular phonons and elastic constants. Inelastic neutron scattering experiments on the high-temperature phase found a significant, though incomplete, softening in the TA₂ phonon branch along the [110] direction, at a wave vector $\mathbf{q}_{PM} \approx \frac{2\pi}{a}(0.33, 0.33, 0)$ (Ref. 3). The phonon softening has been found to correspond to a premartensitic phase occurring between the high-temperature cubic and low-temperature martensitic structures. The premartensitic phase has a cubic structure with a superimposed [110]-transverse shuffling modulation, analogous to the

modulation of the martensitic phase but with a different periodicity of almost 6 interplanar distances.³ While the PM phase is anticipated by a precursor phonon softening at \mathbf{q}_{PM} , no phonon softening at \mathbf{q}_M has been observed above T_M .

The aim of this study is to provide a unified explanation for the microscopic origin of the rich variety of phase transitions and modulated structures occurring in this ferromagnetic shape-memory alloy. To this end we have performed a first-principles study of the phonon dispersions and lattice instabilities of ferromagnetic Ni₂MnGa and of their dependence upon uniform tetragonal strain. In our calculations we use the spin-polarized generalized-gradient approximation (σ -GGA) recently developed within the density-functional perturbation theory (DFPT) formalism.⁹ This approach allows us to obtain an accurate description of the structural, magnetic, and vibrational properties of Ni₂MnGa.

The paper is organized as follows. The details of the computational method are given in section II. In section III we present the results for the cubic Heusler structure. The crystal structure and magnetization are discussed in Section III.A. Section III.B is devoted to the phonon dispersion, with particular attention to the phonon anomaly and related dynamical instability. The origin of the phonon anomaly is discussed in Section III.C. The computed elastic constants are presented and discussed in Section III.D. In Section IV we investigate the dependence of the phonon dispersions and lattice instabilities on uniform tetragonal strain. In Section V the main results are summarized and the microscopic origin of the observed phase transitions explained.

II. COMPUTATIONAL METHOD

Our calculations have been performed within the framework of density-functional and density-functional-perturbation theory (DFT and DFPT). In particular, the vibrational properties have been computed using a recent implementation of ultrasoft pseudopotentials into DFPT.¹⁰ We used ultrasoft pseudopotentials¹¹ for Ni and Mn, freezing the 3*s* and 3*p* core electrons and treating the 3*d* and 4*s* states as valence levels.^{12,13} The nonlinear core correction is used to account for the overlap between the core and the valence charges.¹⁴ For the Ga atom we used a norm-conserving pseudopotential, which also includes a nonlinear core correction, treating the 4*s* and 4*p* states as valence levels. To describe the effects of exchange and correlation, we used the Perdew-Burke-Ernzerhof¹⁵ functional with the spin-polarized generalized gradient correction (σ -GGA), recently implemented within the DFPT formalism in the PWscf code.⁹ For comparison, we have performed calculations within the local spin density approximation (LSDA) using the Perdew-Zunger parameterization of the exchange and correlation energy. The plane-wave basis set had a kinetic-energy cutoff of 25

Ry. The augmentation charges, required by the use of ultrasoft pseudopotentials, were expanded with an energy cutoff of 450 Ry. The Brillouin zone integration was performed using the smearing technique,¹⁶ suitable for metallic systems. The structural properties and most of the phonon frequencies are well converged using a first-order smearing function with a smearing parameter $\sigma=0.03$ Ry and an fcc (6, 6, 6) Monkhorst-Pack grid,¹⁷ yielding 28 \mathbf{k} -points in the irreducible wedge of the Brillouin zone (IBZ) for the cubic structure. To obtain an accurate description of the anomalous TA₂ phonon branch, a smaller smearing parameter is necessary and, consequently, a finer k-point sampling. An accuracy to within a few cm⁻¹ has been obtained using $\sigma=0.01$ Ry and an fcc (10, 10, 10) k-point grid, yielding 110 \mathbf{k} -points in the IBZ, for the cubic structure. For the tetragonal structure, an (8, 8, 8) k-point grid yielding 144 \mathbf{k} -points in the IBZ of the face-centered orthorhombic unit cell was used.

To compute the full phonon dispersions of the cubic structure, we computed the interatomic force constants by Fourier transformation of the dynamical matrices computed on a (6, 6, 6) \mathbf{q} -point grid in the fcc BZ. The phonon dispersions along the [110] ([011]) direction were obtained by interpolating the dynamical matrices computed on a finer mesh of 24 \mathbf{q} -points between Γ and the shortest reciprocal-space vector parallel to the [110] ([011]) direction. An even denser mesh of \mathbf{q} -points has been used in the proximity of the anomaly for a more accurate interpolation of the TA₂ branch.

III. CUBIC Ni₂MnGa

In this section, we report the results of calculations for Ni₂MnGa in the fcc L2₁ Heusler structure (see figure 1).

A. Crystal structure and magnetization

In table I are given the minimum-energy lattice parameter, a_0 , the bulk modulus, B_0 , and the magnetic moment per unit cell, μ_0 , computed within the spin-polarized σ -GGA. Note that to obtain convergence to within $0.01\mu_B$, μ_0 has been computed on a (10, 10, 10) k-point grid with $\sigma=0.01$ Ry. These results agree well with those of all-electron calculations (FLAPW) performed using the σ -GGA.¹⁸ The theoretical results are also in very good agreement with the experimental data; the theoretical lattice parameter obtained with σ -GGA is equal, to within theoretical precision, to the experimental value. For comparison, the LSDA results are included in table I. The LSDA lattice parameter is 2.5% smaller than the experimental value. This underestimate of the lattice parameter is correlated with an increase in the bulk modulus to 38% higher than the experimental value.

B. Phonon dispersion relation

The phonon dispersions of the ferromagnetic cubic structure ($a_0 = 11.03$ a.u.) have been computed, using σ -GGA, for \vec{q} along high-symmetry lines in the first Brillouin zone, as shown in figure 2. The solid lines indicate the computed phonon dispersion converged to within a few wave numbers. The theoretical phonon dispersion curves are in excellent agreement with the available inelastic neutron scattering data.^{4,19}

To evaluate the accuracy of the theoretical method, the phonon frequencies computed using different approximations for the exchange and correlation energy, at the zone boundary X point, are given in table II. Since the experimental frequency of the anomalous ($\zeta\zeta 0$)-acoustic branch is not strongly temperature dependent at this q-point, it is a good reference for evaluating the accuracy of the theoretical method. The experimental frequency for the transverse acoustic mode X₅' is in very good agreement with the phonon frequency computed using the σ -GGA, with the computed value being about 6% softer. For comparison, we have also done the computation with LSDA. Calculations for the cubic structure with the LSDA lattice constant yield frequencies about 10% harder than those computed using the σ -GGA, except for the lowest X₅' mode which is 7% softer, increasing the discrepancy with experiment. In addition, the ordering of the modes in LSDA is different. Specifically, the X₄' mode is softer than the nearby X₅' and X₅ modes. We have also computed the phonon frequencies within the LSDA but fixing the lattice parameter to the equilibrium value computed in the σ -GGA. The result is that all the modes soften, so that the frequencies are about 10% smaller than with σ -GGA. This softening results in an even greater discrepancy with the experimental X₅' mode (20%). We conclude that the better accuracy of σ -GGA is not merely an effect of the more accurate value of the equilibrium lattice parameter. All calculations reported below were performed with σ -GGA.

The most striking feature of the phonon dispersion relation in figure 2 is the anomalous dip in the lowest branch of the transverse acoustic modes (TA₂) along [110]. The minimum at the incommensurate wave vector $\mathbf{q}_0 = \frac{2\pi}{a}(\zeta_0, \zeta_0, 0)$, with $\zeta_0 = 0.34$, is at imaginary frequency. Thus, the crystal is dynamically unstable to the lattice distortion corresponding to the eigenvector of this mode, which consists of a nearly rigid displacement of the (110) atomic planes along the [$\bar{1}\bar{1}0$] direction with a modulation period of slightly less than 6 interplanar distances along the [110] direction. This energy-lowering distortion can be specified by an amplitude, \mathbf{u} , and a phase, ϕ ,

$$\mathbf{u}_m = \mathbf{u} \cos(m\zeta_0\pi + \phi), \quad (1)$$

where \mathbf{u}_m is the displacement of the m^{th} (110) atomic plane along the [$\bar{1}\bar{1}0$] direction. Due to the cubic symmetry, there are 12 equivalent anomalies along the $\langle 110 \rangle$

directions which give rise to six different but crystallographically equivalent lattice modulations \mathbf{u}_m .

The phonon anomaly is shown in more detail in figure 3, where the theoretical dispersion is compared with inelastic neutron scattering data taken at two different temperatures: $T=370$ K (squares) and $T=250$ K (triangles).³ The experimental data display an anomaly in the TA_2 branch that corresponds to the anomaly predicted by our theoretical dispersion. The wave vector of the experimentally-observed anomaly is $\zeta_{PM} \approx 0.33$,³ in excellent agreement with the theoretical value. For those modes that do not have a strong dependence upon temperature, such as the LA branch and the TA_2 modes away from the anomaly ($\zeta \geq 0.45$), the agreement between theory and experiment is very good. To compare theory and experiment for modes that are strongly temperature dependent, we need to extrapolate the experimental values to $T = 0$ K. In accordance with the soft mode theory, $(\hbar\omega)^2$ is experimentally observed to decrease linearly with temperature above $T_{PM}=260$ K. Extrapolation to $T = 0$ K gives an imaginary frequency of $30i$ cm^{-1} , which is in reasonable agreement with the computed value.

Examination of the phonon dispersion throughout the entire BZ shows that imaginary frequencies leading to dynamical instabilities occur only in a very localized region in q -space. This is in agreement with the experimental dispersion measured in the direction perpendicular to \mathbf{q}_0 , $\mathbf{q}=\mathbf{q}_0+(\zeta, -\zeta, 0)$.⁴ The contour plot in figure 4 shows that the lattice instability is confined to a “drop-shaped” small region in reciprocal space, located along the $[110]$ direction and centered at the critical wave vector \mathbf{q}_0 , where the dominant instability occurs. The localized nature of the anomaly in q -space is a signature of its electronic origin, as will be discussed in detail in the next section.

C. Origin of the anomaly

Screening due to electron-phonon coupling involving electronic states near the Fermi level in metals can give rise to anomalous dips in the phonon dispersion, called Kohn anomalies. The occurrence of these anomalies depends mainly on the geometry of the Fermi surface, as well as on the \mathbf{q} -dependence of electron-phonon matrix elements. If the Fermi surface has flat portions with nesting vector \mathbf{q}_0 , there generally will be very strong screening of the potential perturbation due to atomic displacements at that wavevector, leading to a pronounced softening highly localized in q -space. The effect of Fermi surface geometry can be quantified by calculation of the generalized susceptibility, as in Ref. 20.

In cubic Ni_2MnGa , the Fermi level crosses both minority and majority spin bands. Of the two Fermi surfaces, only the one for the minority spin bands, plotted in figure 5, shows obvious nesting features. In particular, a large fraction of the opposite sides of the “pipes,” running

along the faces of the cube and crossing at their center, are nested by wavevectors of the form $(\zeta_0, k, 0)\frac{2\pi}{a}$ with $\zeta_0 = 0.34$ and $0 \leq k \leq 0.34$ and the cubic-symmetry-related equivalent wavevectors. Along $[110]$, this corresponds to the critical wave vector of the anomaly. It should be noted that this differs from the position of the nesting wavevector and peak in generalized susceptibility along $[110]$ found in Refs. 20 and 21. This difference might be attributable to the differences in method, in particular, the difference in choice of density functional. $[110]$ appears to be a direction for which the anomaly is strongest. For example, although there is nesting along $[100]$ as well, there is no sign of an anomaly in the phonon dispersion. This can be attributed to the vanishing of the relevant electron-phonon matrix elements.

The strength of a Kohn anomaly is expected to be very sensitive to electronic temperature, with an increasing temperature reducing the sharpness of the Fermi surface and thus weakening the anomaly. In our calculations, the sensitivity to electronic temperature can be directly investigated, as the smearing parameter σ plays the role of a fictitious electronic temperature. In table III we show the dependence on σ of those modes at the critical wave vector, \mathbf{q}_0 , that have the same symmetry as the soft TA_2 branch (i.e. the three modes of Σ_3 symmetry). The anomalous TA_2 mode, $\Sigma_3(1)$, is much more sensitive to the fictitious electronic temperature than the other two modes. All the frequencies are well converged for $\sigma=0.01$ Ry. The dependence of the phonon anomaly upon the electronic temperature is also shown in figure 2, where the dispersion of the anomalous TA_2 branch computed with $\sigma=0.03$ Ry (dashed line) is compared with the fully converged calculation for $\sigma=0.01$ Ry (solid line). Only the modes with wavevectors close to the anomaly, $(\zeta_0 - 0.16) < \zeta < (\zeta_0 + 0.16)$, are affected by the change in the electronic temperature. The anomaly is smoothed out as the fictitious electronic temperature is increased. Thus, we conclude that the computed dip is indeed a Kohn anomaly.

D. Elastic constants

The computed elastic constants for the ferromagnetic cubic structure are reported in table IV. In a first-principles framework, the standard approach for obtaining elastic constants is to compute the stress tensor for a selected set of small strains. To obtain convergence at the level of a few GPa, we have used very dense k -point meshes (up to $14 \times 14 \times 14$), corresponding to 10976 points in the BZ). To compute C_{11} and C_{12} the cubic crystal is distorted by the tetragonal deformation: $\epsilon_{zz}=\epsilon$, $\epsilon_{xx}=\epsilon_{yy}=0$. For small deformations the stress, σ_{ij} , is linear with ϵ : $\sigma_{xx}=\sigma_{yy}=C_{12}\epsilon$, and $\sigma_{zz}=C_{11}\epsilon$. The values so obtained for the elastic constants C_{11} , C_{12} , and the shear modulus $C'=(C_{11}-C_{12})/2$ are indicated as “theory 1” in table IV.

The small magnitude of C' requires additional attention. We performed an independent computation by considering the tetragonal deformation $\epsilon_{xx}=\epsilon_{yy}=\epsilon$, $\epsilon_{zz}=-2\epsilon$. For small ϵ we have that $\sigma_{xx}=\sigma_{yy}=2C'\epsilon$ and $\sigma_{zz}=-4C'\epsilon$. This direct calculation gives $C'=(2\pm 2)$ GPa, in good agreement with the value obtained as a difference of C_{11} and C_{12} in theory 1. The near-zero value of C' implies that there is almost no energy cost for a small tetragonal shear distortion of the type $2\epsilon_{xx}=2\epsilon_{yy}=-\epsilon_{zz}$. Evidence of this marginal elastic instability towards small volume-preserving tetragonal distortions was also found in Ref. 22, where it was shown that the energy surface as a function of c/a is remarkably flat; specifically, the change in energy associated with varying the c/a ratio in the range of values between 0.97 and 1.01 is almost zero to within numerical accuracy.

In table IV (theory 2) we also show the values of the elastic constants estimated from the slope of the long wavelength acoustic modes along the $[110]$ direction. The elastic constants C_{44} , C' , and $C_L=(C_{11}+C_{12}+2C_{44})/2$ correspond to the TA_1 , TA_2 , and LA modes, respectively. These determine the values of C_{11} and C_{12} given in the table. The evaluation of the elastic constants from the phonon dispersion is less accurate, especially for C' where the corresponding TA_2 branch deviates from a linear behavior already at very small q .

The elastic constants in the high-temperature cubic phase have been experimentally determined between room temperature and the pre-martensitic structural phase transition at $T = 260$ K by measuring the velocity of ultrasonic waves.^{23,24} These experiments show that the elastic constants C_L and C_{11} are almost temperature independent. In contrast, the transverse elastic constants C_{44} and C' exhibit an anomalous behavior with cooling, softening as the pre-martensitic phase transition temperature is approached. While the softening is small for C_{44} , it is more dramatic for C' , which decreases by 60% from room temperature to the transition. We find good agreement between theory and room temperature measurements for C_L and C_{11} , which are not strongly modified by finite temperature. The pronounced softening of C' is also consistent with the very small zero-temperature theoretical value, $C' \approx 0$.

IV. TETRAGONAL Ni_2MnGa

The identification of unstable phonons at $\mathbf{q}_0=\frac{2\pi}{a}(\zeta_0, 0, 0)$, with $\zeta_0 = 0.34$, in the cubic Heusler structure leads naturally to an understanding of the transition to the premartensitic cubic-modulated phase with decreasing temperature. To explore the subsequent transition to the low-temperature martensitic phase with $c/a = 0.94$ and modulation wavevector $\zeta_0 = 0.43$, we extended the calculations of phonon dispersion to Heusler structures with uniform volume-preserving tetragonal strains ranging from $c/a = 0.88$ to $c/a = 1.06$, with particular atten-

tion to the TA modes along the $\langle 110 \rangle$ directions.

A. Tetragonal structure with $c/a=0.94$

We first consider in detail the volume-preserving tetragonal distortion with $c/a=0.94$, corresponding to the low temperature martensitic phase. The phonon dispersions computed along the inequivalent $[110]$ and $[011]$ directions of the tetragonal BZ are shown in figure 6. The only mode substantially affected by the tetragonal distortion is the anomalous TA_2 mode. We find an overall softening (hardening) of the TA_2 branch in the $[110]$ ($[011]$) direction. The anomaly is particularly affected by the tetragonal distortion. Along the $\langle 110 \rangle$ directions, which are perpendicular to the c axis, the phonon anomaly is more pronounced and is shifted to a larger q -vector ($\zeta = 0.43$) than in the cubic structure. This wavevector is in excellent agreement with the long period modulation observed experimentally in the tetragonal martensitic phase. In contrast, along the $\langle 011 \rangle$ directions, the anomaly has almost completely disappeared; the entire branch is stable and there is only a very small wiggle in the TA_2 branch. Thus, the entropy from low-frequency phonons should be roughly a factor of three less than in the premartensitic phase, which may explain why the premartensitic phase is more favorable at higher temperatures.

As in the cubic phase, the anomaly can be associated with features of the Fermi surface. In figure 7 we show the minority-spin Fermi surface computed for Ni_2MnGa in the tetragonal structure. It is related to the Fermi surface of the cubic structure with two major differences: (i) there are no flat surfaces perpendicular to the (001) direction, and (ii) the “pipes” running along the faces of the tetragonal BZ are wider than the corresponding features in the cubic Fermi surface. As a consequence of these changes, induced by the tetragonal distortion, there is significant nesting only in the $\langle 110 \rangle$ directions perpendicular to the c axis and the edges of the “pipes” are nested by the larger ($\zeta \zeta 0$) critical wave-vector, $\zeta = 0.43$. This explains why in the tetragonal structure there are pronounced Kohn anomalies only in the $\langle 110 \rangle$ directions, at a larger wave vector than in the cubic structure.

B. Evolution of phonon anomaly with tetragonal deformation

To understand better the lattice instabilities and related structural energetics of Ni_2MnGa , we studied the evolution of the TA_2 phonon anomaly with uniform volume-preserving tetragonal strain.

Studying the phonon dispersions of the cubic Heusler structure ($c/a = 1$) and its tetragonal distortion with $c/a = 0.94$, we have identified the existence of the unstable mode at $\zeta = 0.34$ and $\zeta = 0.43$, respectively, that

explain the transitions to the premartensitic and martensitic phases with decreasing temperature. The fact that for the two tetragonal strains the soft mode is always the TA_2 mode but with a different wave vector suggests that the wavevector of the soft mode and the tetragonal strain are coupled. We therefore studied in more detail the dependence of ζ upon tetragonal strain.

The dispersion of the TA_2 branch along the $[110]$ direction is shown in figure 8 for several values of the c/a ratio. An overall softening of the TA_2 branch is observed with decreasing c/a ratio. With compressive strain ($c/a < 1$) the anomaly occurs at a larger ζ_0 than in the cubic structure, and becomes broader and more pronounced. For $c/a \lesssim 0.91$ the entire branch is unstable. With tensile strain ($c/a > 1$) the anomaly shifts to a smaller ζ_0 and becomes less pronounced. The lattice instability is completely eliminated for $c/a \gtrsim 1.06$. This is in agreement with the experimental observation of no superimposed modulations in a stress induced tetragonal phase with $c/a = 1.18$.²⁵

In figure 8, we have shown the TA_2 branch for several different values of c/a . For each of these values of c/a , we can find the value of the wavevector ζ_0 for which the imaginary frequency of the TA_2 branch has its minimum. This gives us the dependence of the modulation wavevector upon strain and is shown in figure 8. Three regimes can be identified: (i) $c/a \lesssim 0.91$, where the entire TA_2 branch is unstable and there is no unique minimum; (ii) $0.9 < c/a < 1.06$, where the TA_2 branch displays a well-defined dynamical instability localized at the wavevector ζ_0 that depends on c/a ; and (iii) $c/a \gtrsim 1.06$, where the lattice instability is completely eliminated and the TA_2 branch is stable over the whole BZ, so that no minimum is defined. Only in regime (ii) can a modulated structure be expected to occur.

In order to quantify these trends, in figure 10 we decompose the phonon frequency ω^2 into a short-range “normal” part ω_n^2 and a long-range “anomalous” part ω_a^2 : $\omega^2(\zeta) = \omega_n^2(\zeta) + \omega_a^2(\zeta)$. The “normal” contribution, defined as $\omega_n^2(\zeta) = A[1 - \cos(\zeta\pi)]$, depends only upon short-range interatomic force constants and is connected to the local chemistry of the crystal. It corresponds to the simple model for the transverse $[1\bar{1}0]$ vibrations of the $[110]$ planes when they interact only with a first-neighbor interplanar force constant: $K = -Am/2$, where m is the mass associated with each plane. The long-range “anomalous” contribution ω_a^2 depends on electronic screening effects that can be strongly \mathbf{q} dependent. To fit the constant A in the definition of $\omega_n^2(\zeta)$, we assume that for $\zeta=1$ the anomalous contribution is zero.

The short-range contribution softens with decreasing c/a ratio, causing the overall softening observed for the TA_2 branch. Decreasing c/a corresponds to a volume-preserving tetragonal distortion with a shorter c and larger a . Therefore smaller c/a values correspond to a larger $[110]$ interplanar distance which leads to a weaker interplanar force constant and therefore a softer ω_n^2 .

The anomalous contribution ω_a^2 is negative, large, and

peaked at a critical wave vector ζ_0 , indicating a strong screening due to the electron-phonon coupling and Fermi surface nesting. Both ζ_0 and the intensity of the anomaly are strongly dependent upon strain. The value of ζ_0 increases with decreasing c/a , the intensity reaching its maximum at $c/a=0.97$.

V. SUMMARY AND CONCLUSIONS

Our ab initio study of the phonon dispersion and lattice instabilities in cubic and tetragonal Ni_2MnGa can be summarized as follows.

First, the parent cubic phase exhibits a marginal elastic instability, $C' \approx 0$, meaning that there is almost no energy cost for a small uniform tetragonal distortion.

Second, for $0.91 < c/a < 1.06$ a Kohn anomaly is present due to electron-phonon coupling and Fermi surface nesting. It develops into a deep minimum corresponding to a localized dynamical instability whose wave vector ζ_0 is related in a one-to-one fashion to the c/a ratio. Therefore, tetragonal structures with c/a in this range are unstable towards a particular transverse (110)-shuffling modulation with a specific wavevector ζ_0 , the one-to-one relationship of the c/a ratio and the modulation period being due to the behavior of the topology of the Fermi surface under tetragonal distortions.

Consequently, the energy of the cubic structure may be lowered by any one of a family of deformations, $\{\epsilon, \mathbf{u}(\zeta_\epsilon)\}$, consisting of a tetragonal strain, ϵ , and a superimposed (110)-shuffling modulation, $\mathbf{u}(\zeta_\epsilon)$, whose periodicity, ζ , is directly related in a one-to-one fashion to the c/a ratio.

The near-vanishing of C' together with the fact that the energy surface as a function of c/a is remarkably flat permits a modulated ground state with c/a significantly different from 1. Indeed, the computed relation between c/a and the modulation wavevector is in excellent agreement with structural data on the premartensitic ($c/a = 1$) and martensitic ($c/a = 0.94$) phases of Ni_2MnGa , and also with the unmodulated stress-induced phase ($c/a = 1.18$).

The next step is to carry out total energy calculations of the complex modulated structures in order to determine the equilibrium amplitude and phase of the lattice modulation and the associated energy gain. The energy could then be expanded in terms of symmetry invariants of the relevant structural degrees of freedom (strain and modulation) and determine the coefficients of each term of the expansion using ab initio calculations. In this way one could develop an ab-initio based finite-temperature statistical model of the phase transition in Ni_2MnGa .

The three phases of Ni_2MnGa observed with increasing temperature can be understood as follows. At low temperatures, a minimum-energy modulated tetragonal structure is expected, consistent with the observed $c/a = 0.94$ phase. As temperature increases, the favorable entropy arising from the larger phase space for the low-

frequency phonons in the cubic structures leads to a phase transition to the cubic-modulated structure, with a modulation wavevector shifted down from that in the tetragonal phase in accordance with our results. Finally, the frequencies of the unstable phonons associated with the modulation are anharmonically renormalized at the highest temperatures and the observed structure is the cubic Heusler structure, with large fluctuating local distortions.

In conclusion, we have provided a first-principles microscopic explanation for the origin of the physically interesting and technologically important martensitic phase transitions in the ferromagnetic shape-memory Heusler alloy Ni₂MnGa.

Calculations in this work have been done using the PWscf package.²⁶ We thank Morrel Cohen, Richard James and Xiangyang Huang for valuable discussions, and Vitaly Godlevsky for his help in the early stages of this work.

* Current email: bungaro@physics.rutgers.edu

¹ S. J. Murray, M. A. Marioni, A. M. Kukla, J. Robinson, R. C. O'Handley, and S. M. Allen, *J. Appl. Phys.* **87**, 5774 (2000).

² A. Sozinov, A. A. Likhachev, N. Lanska, and K. Ullakko, *Appl. Phys. Lett.* **80**, 1746 (2002).

³ A. Zheludev, S. M. Shapiro, P. Wochner, A. Shwartz, M. Wall, and L. E. Tanner, *Phys. Rev. B* **51**, 11310 (1995).

⁴ A. Zheludev, S. M. Shapiro, P. Wochner, and L. E. Tanner, *Phys. Rev. B* **54**, 15045 (1996).

⁵ P. J. Webster, K. R.A. Ziebeck, S. L. Town, and M. S. Peak, *Philos. Mag.* **49**, 295 (1984).

⁶ V. V. Martynov and V. V. Kokorin, *J. Phys. (France) III* **2**, 739 (1992).

⁷ R. Tickle and R. D. James, *J. Magn. Mater* **195**, 627 (1999).

⁸ V. Buchelnikov, A. Zayak, A. Vasilev and T. Takagi, *Int. J. Appl. Electromag. and Mech.* **12**, 19 (2000).

⁹ A. Dal Corso and S. de Gironcoli, *Phys. Rev. B* **62**, 273 (2000).

¹⁰ A. Dal Corso, A. Pasquarello, and A. Baldereschi, *Phys. Rev. B* **56**, 11 369 (1997).

¹¹ D. Vanderbilt, *Phys. Rev. B* **41**, 7892 (1990).

¹² The details for the Ni pseudopotential can be found in Ref. 9.

¹³ We generated the pseudopotential for Mn, using as reference the all-electron configuration $3d^5, 4s^2$. The core radii are (in a.u.): $4s$ (2.0, 2.2), $4p$ (2.2, 2.4), $3d$ (1.6, 2.2). The all electron potential pseudized inside $r_c=1.8$ has been taken as a local potential. Two values of the core radii indicate a channel which has been pseudized with the ultrasoft scheme. In such a case the first value is the norm-conserving core radius and the second is the ultrasoft one.

¹⁴ S. Louie, S. Froyen and M. L. Cohen, *Phys. Rev. B* **26**, 1738 (1982).

¹⁵ J. P. Perdew, K. Burke, and M. Ernzerhof, *Phys. Rev. Lett.* **77**, 3865 (1996).

¹⁶ M. Methfessel and A. T. Paxton, *Phys. Rev. B* **40**, 3616 (1989).

¹⁷ H. J. Monkhorst and J. D. Pack, *Phys. Rev. B* **13**, 5188 (1976).

¹⁸ A. Ayuela, J. Enkovaara, K. Ullakko, and R. M. Nieminen, *J. Phys. Condens. Matter* **11**, 2017 (1999).

¹⁹ A. Zheludev, S.M. Shapiro, P. Wochner, A. Shwartz, M. Wall, and L. E. Tanner, *J. Phys. IV Colloq.* **5**, C8-1139 (1995).

²⁰ Y. Lee, J. Y. Rhee and B. N. Harmon, *Phys. Rev. B* **66**, 054424 (2002).

²¹ O. I. Velikokhatny and I. I. Naumov, *Phys. Solid State* **41**, 617 (1999).

²² See Figure 1 in: V. V. Godlevsky and K.M. Rabe, *Phys. Rev. B* **63**, 134407 (2001).

²³ J. Worgull, E. Petti, and J. Trivisonno, *Phys. Rev. B* **54**, 15695 (1996).

²⁴ L. Mañosa, A. González-Comas, E. Obradó, A. Planes, V. A. Chernenko, V. V. Kokorin, and E. Cesari, *Phys. Rev. B* **55**, 11068 (1997).

²⁵ V. V. Martynov, *J. Phys. (France) IV* **C8**, 91 (1995).

²⁶ S. Baroni, A. Dal Corso, S. de Gironcoli, and P. Giannozzi, <http://www.pwscf.org>.

²⁷ P. J. Webster, *Contemp. Phys.* **10**, 559 (1969).

TABLE I. Equilibrium lattice parameter, a_0 , bulk modulus, B_0 , and magnetic moment, μ_0 , for Ni_2MnGa in the $L2_1$ Heusler structure. Calculations using the spin-polarized GGA (σ -GGA), are compared with experimental data and with the results obtained using LSDA.

	a_0 (a.u.)	B_0 (Mbar)	μ_0 (μ_B)
σ -GGA	11.03	155	4.27
LSDA	10.74	202	3.92
FLAPW- σ -GGA ^c	10.98	156	4.09
Exp.	11.01 ^a	146 ^b	4.17 ^a

^aRef. 27

^bRef. 23

^cRef. 18

TABLE II. Phonon frequencies (in cm^{-1}) computed at the zone-boundary point X. Results obtained using different approximations for the exchange and correlation energy, σ -GGA and LSDA, are compared with the experiment.

a_0	σ -GGA	LSDA	LSDA	Exp.
	a_0 (σ -GGA)	a_0 (LSDA)	a_0 (σ -GGA)	
X_5'	82	76	70	87
X_1'	160	179	151	
X_5	174	191	161	
X_5'	176	195	166	
X_4'	178	185	159	
X_1	191	203	168	
X_1'	227	249	212	
X_5'	259	286	233	

TABLE III. Dependence upon the smearing parameter, σ , of the frequency of the three Σ_3 -modes at the critical wavevector, \mathbf{q}_0 . The $\Sigma_3(1)$ mode is the anomalous TA_2 mode, the other two, $\Sigma_3(2)$ and $\Sigma_3(3)$, are higher frequency optical modes. The \mathbf{k} -point mesh needed to achieve convergence for each of the values of σ is also reported. Frequencies are in cm^{-1} .

σ (Ry)	\mathbf{k} -mesh	$\Sigma_3(1)$	$\Sigma_3(2)$	$\Sigma_3(3)$
0.03	(6 6 6)	8	195	244
0.01	(10 10 10)	39i	195	242
0.005	(12 12 12)	39i	195	242

TABLE IV. Elastic constants, in GPa, for ferromagnetic Ni_2MnGa in the cubic Heusler structure. Theory 1, elastic constants from stress calculation under strain. Theory 2, elastic constants estimated from the slope of the $[\zeta\zeta 0]$ acoustic branches close to Γ : C' , C_{44} , and C_L correspond to the TA_2 , TA_1 , and LA modes, respectively. Room temperature measurements are shown for comparison.

	C_{11}	C_{12}	C'	C_{44}	C_L
theory 1	153 ± 2	148 ± 2	2.5 ± 2		
theory 2	138 ± 9	143 ± 9	-2.5 ± 5	100 ± 5	240 ± 5
Exp. ^a	152	143	4.5	103	250
Exp. ^b	136 ± 3	–	22 ± 2	102 ± 3	222 ± 9

^aRef. 23

^bRef. 24

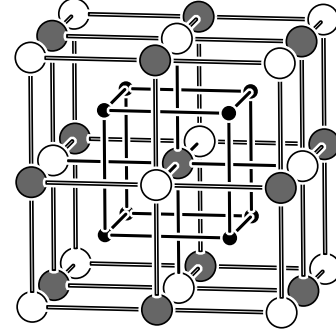


FIG. 1. The fcc $L2_1$ Heusler structure of Ni_2MnGa . The small circles, large open circles and large filled circles represent Ni, Mn and Ga, respectively.

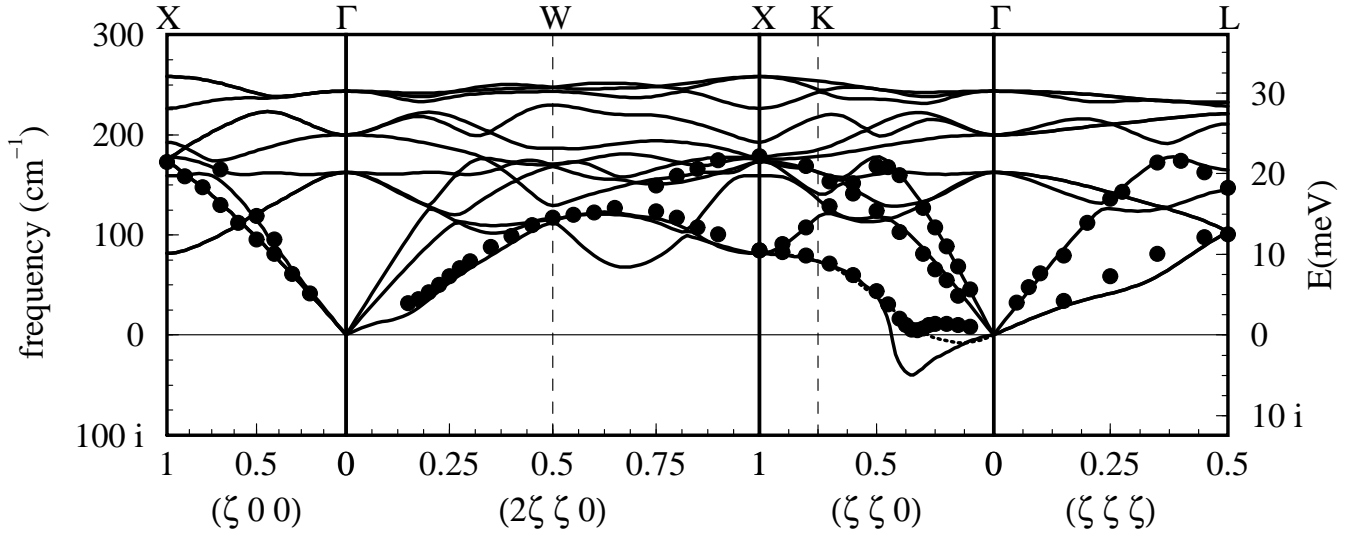


FIG. 2. Full phonon dispersion of ferromagnetic Ni_2MnGa in the fcc Heusler structure, along high symmetry lines of the fcc BZ. Solid lines are fully converged ab initio calculations obtained using an effective electronic temperature $\sigma=0.01\text{Ry}$. The dashed line is the dispersion obtained using a higher effective electronic temperature, $\sigma=0.03\text{Ry}$, showing the dependence of the anomaly in the lowest acoustic branch along the $(\zeta\zeta 0)$ direction on the effective electronic temperature. The circles indicate the neutron scattering data from Refs. [19, 4]. The imaginary values of phonon frequencies are plotted along the negative frequency axis. The wave-vector coordinate ζ is in units of $\frac{2\pi}{a}$.

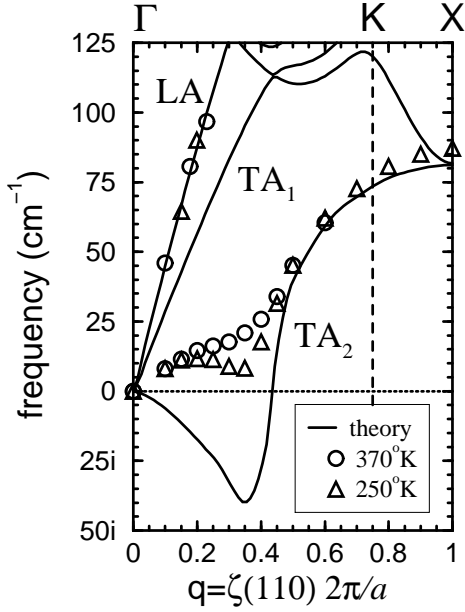


FIG. 3. Partial phonon dispersion of Ni_2MnGa in the fcc Heusler structure, along the Γ -K-X line in the $[110]$ direction. The theoretical data are the same as in figure 2. The experimental data taken at 250 K and 270 K are shown for comparison.

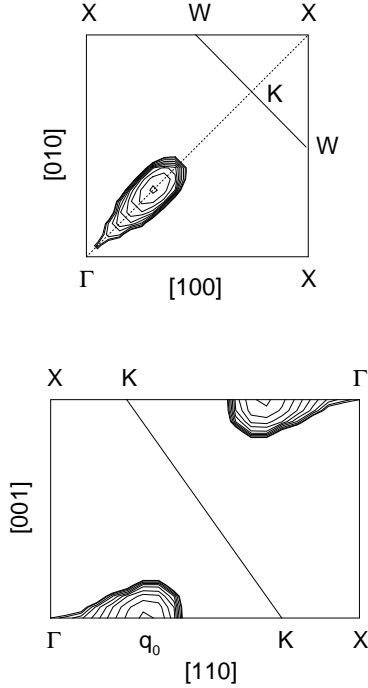


FIG. 4. Contour plots of the imaginary phonon frequencies in the (001) plane (a) and $(\bar{1}\bar{1}0)$ plane (b) of the fcc BZ. These contour plots show the region in q -space where the crystal is dynamically unstable. This occurs in a narrow valley situated along the $[110]$ direction with its minimum at the critical wave vector $\mathbf{q}_0=(0.34, 0.34, 0)$.

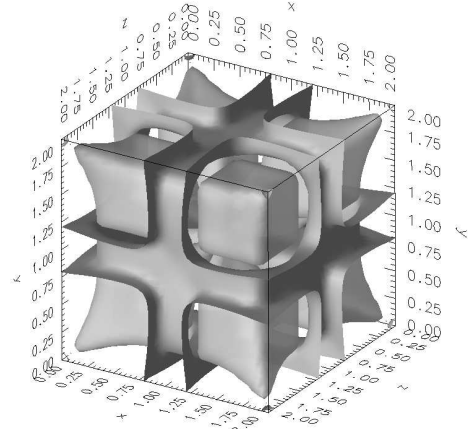


FIG. 5. Fermi surface of minority spin bands for cubic Ni_2MnGa .

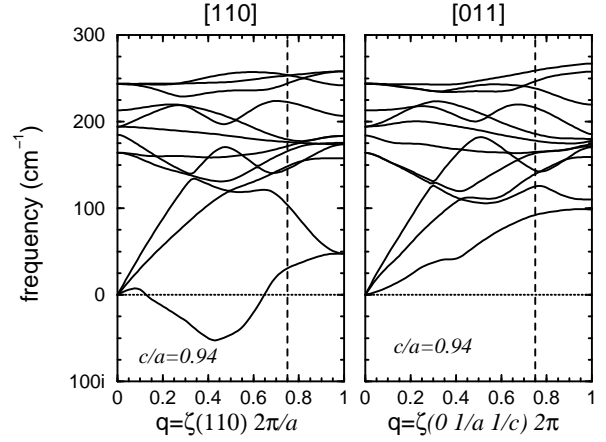


FIG. 6. Ab initio $[110]$ and $[011]$ phonon dispersions for ferromagnetic Ni_2MnGa in the tetragonal structure ($c/a=0.94$, $a=11.26$ a.u.).

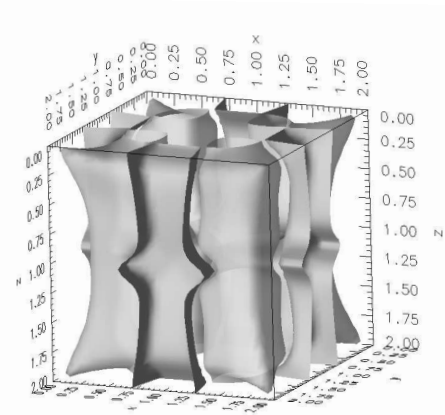


FIG. 7. Fermi surface of minority spin bands for tetragonal Ni_2MnGa ($c/a=0.94$).

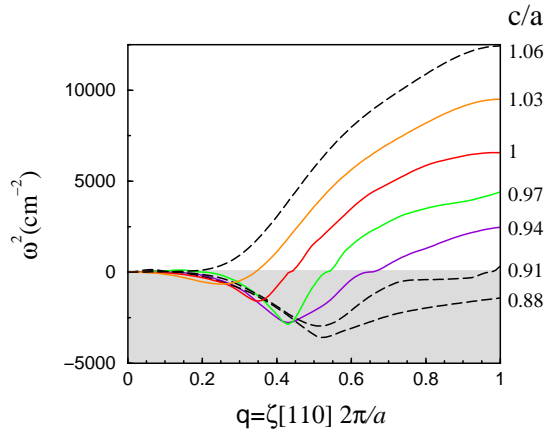


FIG. 8. (color online only). Dispersion of the squared frequencies, for the anomalous TA_2 phonon branch, computed for different volume-preserving tetragonal distortions, with c/a ranging from 0.88 to 1.06.

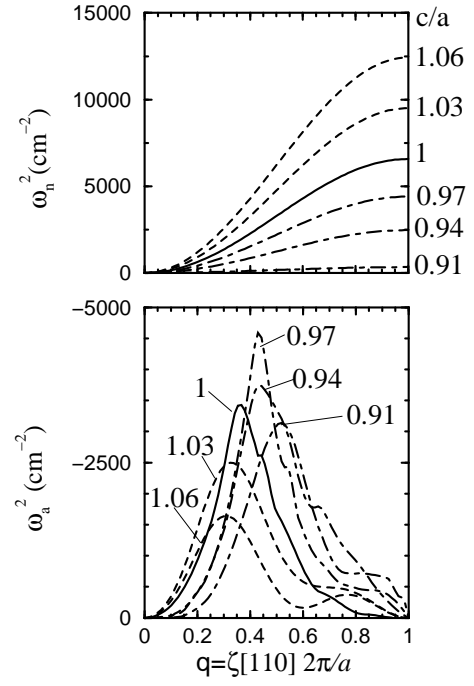


FIG. 10. Decomposition of ω^2 into “normal” (ω_n^2) and anomalous (ω_a^2) parts for different volume-preserving tetragonal distortions, with c/a varying from 0.91 to 1.06. Dashed lines are for $c/a > 1$, dot-dashed lines are for $c/a < 1$ and solid lines are for $c/a = 1$.

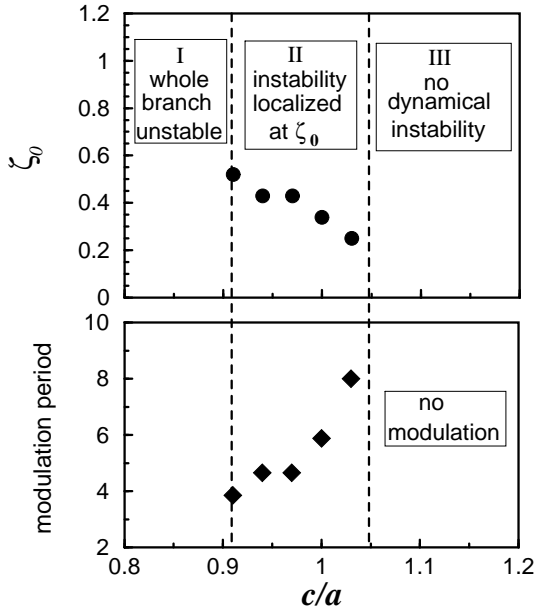


FIG. 9. Dependence upon c/a of the modulation wavevector ζ_0 and the related modulation period (in unit of (110) interplanar distances).